### Part III

# Scattering and Absorption Properties of Small Particles and Illustrative Applications

There are two classes of problems involving electromagnetic scattering by small particles: the direct problem and the inverse problem. Thus far, we have dealt primarily with the direct problem of calculating or measuring the scattering by a known, well-defined system. The so-called inverse problem is to characterize a system of interest using scattering data collected from laboratory measurements or remote sensing observations.

Given the unlimited diversity of particle types in nature and in the laboratory, one may expect a significant variability in the optical properties of particles encountered in different applications. Therefore, solving the inverse problem may often be facilitated by previous knowledge of how the various absorption and scattering properties of small particles may depend on the particle size parameter, morphology, relative refractive index, and orientation. This knowledge may be the cumulative result of analyzing many specific cases supplemented by careful interpolation or extrapolation to the range of particle characteristics not specifically covered by existing theoretical or experimental results.

The purpose of the following two chapters is to discuss the current understanding of the optical properties of small particles. Although we have not attempted an exhaustive summary of all published results, we hope that these chapters will provide useful information to those interested in a preliminary qualitative or semi-quantitative analysis of a specific problem as well as to those evaluating the feasibility of a more precise quantitative solution and considering various solution approaches. We also discuss a few selected applications which demonstrate the great potential of electromagnetic scattering as a noninvasive particle characterization and remote sensing tool.

### Chapter 9

## Scattering and absorption properties of spherical particles

The decisive advantages of the Lorenz–Mie theory compared to any other theoretical technique are its unparalleled numerical accuracy, high computational efficiency, and applicability to essentially any size parameter and relative refractive index. These attributes permit a comprehensive study of electromagnetic scattering by at least one class of small particles, viz., isotropic and homogeneous spheres. Although a substantial fraction of the particles encountered in natural and laboratory conditions are nonspherical, the Lorenz–Mie theory provides a first-order description of many optical effects that are common to all small particles and may not be intuitively obvious. Furthermore, there are many practical situations in which the scattering particles in question are almost, if not precisely, spherical so that the Lorenz–Mie theory can be expected to apply directly. Hence our approach is to begin by a detailed analysis of the scattering and absorption properties of spherical particles and continue, in the following chapter, with a discussion of the effects caused by particle nonsphericity. All numerical data discussed in this chapter have been computed using the Lorenz–Mie code described in Section 5.10 and the ray-tracing code described by Macke and Mishchenko (1996).

### 9.1 Monodisperse spheres

Two properties of the extinction efficiency factor  $Q_{\rm ext}$  make it often a more convenient quantity to display than the extinction cross section. First,  $Q_{\rm ext} = C_{\rm ext}/(\pi r^2)$  is a function of the dimensionless size parameter  $x = 2\pi r/\lambda_1$  (subsection 5.8.2), whereas the extinction cross section  $C_{\rm ext}$  itself depends on both the particle radius, r, and the wavelength in the surrounding medium,  $\lambda_1$ . Second, Eq. (7.12) shows that, in the

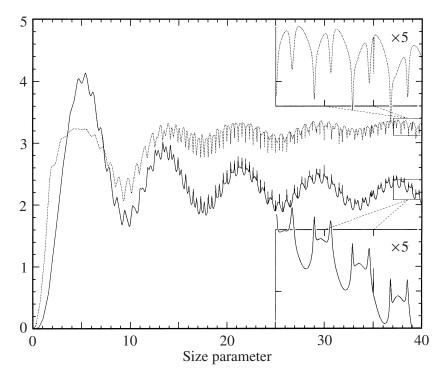


**Figure 9.1.** Extinction efficiency factor  $Q_{\text{ext}}$  (solid curve) and asymmetry parameter  $\langle \cos \Theta \rangle$  multiplied by a factor of 4 (dotted curve) versus size parameter x for monodisperse spherical particles with a relative refractive index m = 1.4.

large-particle limit,  $C_{\rm ext}$  is proportional to the second power of r and hence may span many orders of magnitude, depending on the range of particle radii displayed, whereas the asymptotic value of  $Q_{\rm ext}$  is 2 and its maximum value is often not much greater than the asymptotic value.

The solid curve in Fig. 9.1 shows the extinction efficiency factor  $Q_{\rm ext}$  as a function of size parameter for monodisperse spherical particles with a relative refractive index m=1.4, and the dotted curve depicts the asymmetry parameter  $\langle\cos\Theta\rangle$ . Since the imaginary part of the relative refractive index is here set at zero, the scattering efficiency factor is equal to the extinction efficiency factor, the absorption efficiency factor is equal to zero, and the single-scattering albedo is equal to unity. In agreement with Eqs. (7.3), (7.7), and (7.12), both  $Q_{\rm ext}$  and  $\langle\cos\Theta\rangle$  rapidly vanish as x approaches zero, and  $Q_{\rm ext}$  tends to its asymptotic value 2 as  $x\to\infty$ . In the intermediate (so-called resonance) region of size-parameter values, the extinction efficiency factor can exceed the geometrical optics value, 2, especially as the real part of the relative refractive index is increasing (cf. Fig. 9.2).

Both curves in Fig. 9.1 are characterized by a succession of major low-frequency maxima and minima with superimposed high-frequency ripples composed of sharp, irregularly spaced extrema, some of which are super-narrow spike-like features. The major maxima and minima are called the "interference structure" since, as traditionally explained, they are the result of interference of the light diffracted and

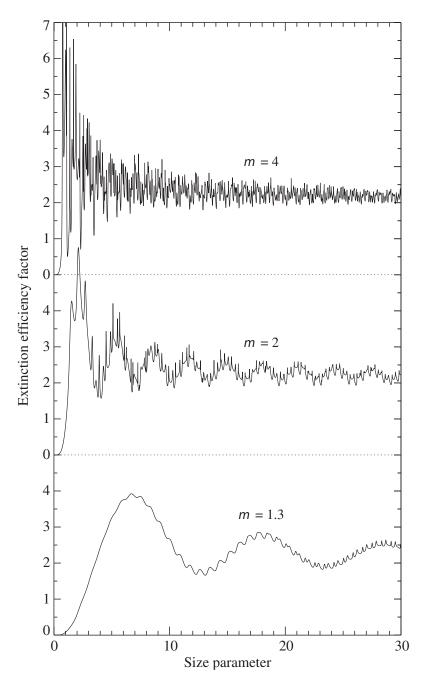


**Figure 9.2.** Extinction efficiency factor  $Q_{\text{ext}}$  versus size parameter x for monodisperse spherical particles with relative refractive indices m = 1.3, 2, and 4.

transmitted by the particle (van de Hulst 1957; Chýlek and Zhan 1989; Lock and Yang 1991). A light ray passing through the center of a sphere acquires a phase shift  $\rho = 2x(m_R - 1)$ , where  $m_R$  is the real part of the relative refractive index. Therefore, constructive and destructive interference and, thus, maxima and minima in the extinction efficiency curve, occur successively at intervals  $\approx 2\pi$  in  $\rho$  (see Fig. 9.3, which shows  $Q_{\rm ext}$  as a function of  $\rho$  for monodisperse spheres with various real

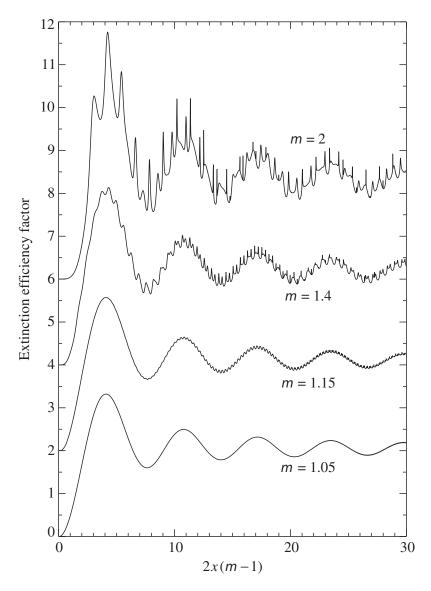


**Figure 9.3.** Extinction efficiency factor versus phase shift for monodisperse spherical particles with relative refractive indices m = 1.05, 1.15, 1.4, and 2. The vertical scale applies to the curve for m = 1.05, the other curves being successively displaced upward by 2.

relative refractive indices). With  $m_R \to \infty$ , the central transmitted rays are increasingly attenuated by the external reflection, and the interference structure becomes less pronounced (cf. Fig. 9.2) and ultimately disappears (Chýlek and Zhan 1989).

Unlike the interference structure, the ripple is caused by the resonance behavior of the Lorenz-Mie coefficients  $a_n$  and  $b_n$  (see, e.g., the review by Hill and Benner (1988) and references therein). The resonances in lower-order coefficients are relatively broad and often overlap. As n increases, the resonance features become narrower, and starting with  $n \sim 20$  (for m = 1.4) each feature in the ripple structure can be identified with an individual resonance in the corresponding partial coefficient  $a_n$  or  $b_n$ . As the size parameter approaches a resonant value, the denominator of a Mie

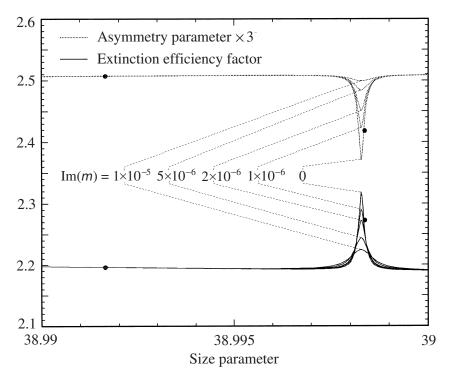
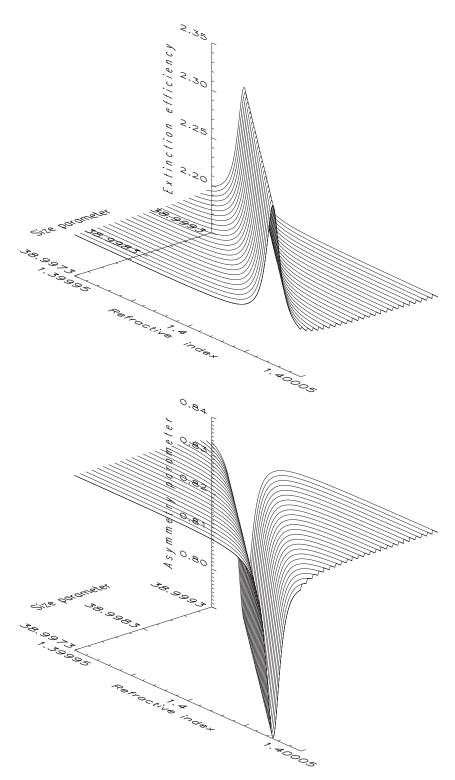


Figure 9.4. Profile of the resonance centered at  $x \approx 38.9983$  for  $m_R = 1.4$  and five values of  $m_I$ . The dots show the sampling resolution used in Fig. 9.1.

coefficient  $a_n$  or  $b_n$  approaches a local minimum, thereby causing a local extremum (maximum or minimum) in the curve for a specific scattering characteristic. Accordingly, the numbers of spike-like extrema in the two curves in Fig. 9.1 are identical, and a sharp local maximum in the extinction curve always corresponds to a sharp local minimum in the asymmetry parameter curve. Some of the resonance features can be extremely narrow. This is demonstrated in Fig. 9.4, which shows the angular profile of the resonance centered at  $x \approx 38.9983$ . The dots indicate the sampling resolution used in Fig. 9.1, illustrating that it is just coincidence that the resonance depicted in Fig. 9.4 is resolved in Fig. 9.1.

Figure 9.5 demonstrates that the resonance features shown in Fig. 9.4 are not simply an isolated peak in  $Q_{\rm ext}$  and an isolated hollow in  $\langle \cos \Theta \rangle$ . Instead, Fig. 9.4 depicts merely a cross section (corresponding to m=1.4) of a long crest and a colocated long canyon appearing in the surface plots of  $Q_{\rm ext}$  and  $\langle \cos \Theta \rangle$ , respectively, as functions of size parameter and real relative refractive index. It is interesting that the middle of the crest and the middle of the canyon in Fig. 9.5 follow the curves mx = constant. This means that, for a given resonance, increasing the relative refractive index shifts the location of the maximum in  $Q_{\rm ext}$  (and the minimum in  $\langle \cos \Theta \rangle$ ) towards smaller size parameters.

It is straightforward to show (Chýlek 1973; Probert-Jones 1984) that the Lorenz–Mie coefficients given by Eqs. (5.219) and (5.220) can be expressed as



**Figure 9.5.** High-resolution surface plots of the extinction efficiency factor and asymmetry parameter versus size parameter and relative refractive index for monodisperse nonabsorbing spherical particles.

$$a_{n}(x,m) = \frac{p_{n}(x,m)}{p_{n}(x,m) + iq_{n}(x,m)}$$

$$= \frac{[p_{n}(x,m)]^{2}}{[p_{n}(x,m)]^{2} + [q_{n}(x,m)]^{2}} - i\frac{p_{n}(x,m)q_{n}(x,m)}{[p_{n}(x,m)]^{2} + [q_{n}(x,m)]^{2}},$$
(9.1)

$$b_n(x, m) = \frac{r_n(x, m)}{r_n(x, m) + is_n(x, m)}$$

$$= \frac{[r_n(x,m)]^2}{[r_n(x,m)]^2 + [s_n(x,m)]^2} - i \frac{r_n(x,m) s_n(x,m)}{[r_n(x,m)]^2 + [s_n(x,m)]^2},$$
(9.2)

where

$$p_n(x, m) = m \psi_n(mx) \psi'_n(x) - \psi_n(x) \psi'_n(mx),$$
 (9.3)

$$q_n(x, m) = -m\psi_n(mx)\chi'_n(x) + \chi_n(x)\psi'_n(mx),$$
 (9.4)

$$r_n(x, m) = m\psi_n(x)\psi'_n(mx) - \psi_n(mx)\psi'_n(x), \tag{9.5}$$

$$s_n(x, m) = -m\chi_n(x)\psi'_n(mx) + \psi_n(mx)\chi'_n(x),$$
 (9.6)

and  $\chi_n(x) = -xy_n(x)$  (cf. Eqs. (5.218) and (C.1)). The convenience of writing  $a_n(x, m)$  and  $b_n(x, m)$  in this form is that the functions  $p_n(x, m)$ ,  $q_n(x, m)$ ,  $r_n(x, m)$ , and  $s_n(x, m)$  are real if the relative refractive index is real. The denominators of Eqs. (9.1) and (9.2) can vanish completely only for complex size parameters, whereas for real size parameters they always remain finite. Therefore, what happens at a resonance is that either  $q_n(x, m)$  or  $s_n(x, m)$  vanish. For this specific set of x-, x-, and x-values, the real part of x-, x-, or x-, or x-, and x-values, the imaginary part vanishes (Chýlek 1976). Accordingly, quantities like Re x-, x-, and x-

$$-m\psi_{n}(mx)\chi'_{n}(x) + \chi_{n}(x)\psi'_{n}(mx) = 0$$
 (9.7a)

or

$$-m\chi_{n}(x)\psi'_{n}(mx) + \psi_{n}(mx)\chi'_{n}(x) = 0.$$
 (9.7b)

Note that for given n and m, these equations have infinitely many solutions at discrete values of x.

Another way to look at resonances is to consider the complex size-parameter plane (though still with the restriction of a real relative refractive index) and write  $a_n(x, m)$  or  $b_n(x, m)$  as a simple pole, e.g.,

$$a_n(x,m) = \frac{\alpha}{x-z},\tag{9.8}$$

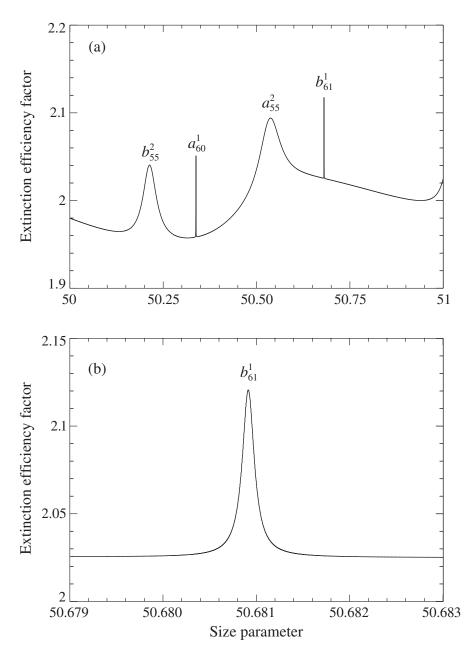
where z is the position of the pole and  $\alpha$  is the residue (Conwell *et al.* 1984; Hunter *et al.* 1988). The resonant size parameter is then given by the real part of z.

A physical interpretation of resonances is that of a situation where rays propagate around the inside surface of a spherical particle, confined by an almost total internal reflection (Hill and Benner 1988): the rays approach the internal surface at an angle beyond the critical angle and are totally reflected each time. After propagating around the sphere, the rays return to their respective entrance points exactly in phase and then follow the same path all over again without being attenuated by destructive interference. Therefore, it takes longer for the electromagnetic energy of the rays to leak out of the sphere, and very large energy densities can be accumulated inside the particle near its surface. Since the accumulated energy is removed from the incident beam, the result of the resonance process is an increased extinction efficiency of the particle. It can be shown that the longer the internal path of the rays, the narrower the resonance (e.g., Roll and Schweiger 2000).

For a fixed m and each index n, there is a sequence of resonance x-values for either  $a_n(x, m)$  or  $b_n(x, m)$ . Hence it is convenient to label each local extremum with the type of mode causing the resonance (a or b), the subscript n, and a superscript l indicating the sequential order of x (Chýlek 1976; Chýlek et al. 1978). This labeling convention is illustrated in the upper panel of Fig. 9.6, which shows the resonance extinction features for a water droplet within the interval  $x \in [50, 51]$ . The main traits of the resonance features are that their width decreases as n increases for a given n and their width increases as n increases for a given n. For n greater than about 50, the n resonance can become extremely narrow, as demonstrated in the lower panel of Fig. 9.6.

Figure 9.4 shows the behavior of the super-narrow resonance centered at  $x \approx$ 38.9983 (for m = 1.4) with increasing imaginary part of the relative refractive index  $m_{\rm L}$ . It is seen that raising  $m_{\rm L}$  from 0 to a very small value of  $10^{-5}$  almost completely destroys this spike-like feature while causing no change whatsoever in the background  $Q_{\rm ext}$  and  $\langle \cos \Theta \rangle$  values. It takes significantly greater  $m_{\rm I}$ -values to eliminate the broader resonances and still greater values (of order 0.1) to eliminate the interference structure (Figure 9.7). This is not surprising. Indeed, the diffracted rays are unaffected by absorption, whereas attenuation of the transmitted rays gives weaker interference in the near-forward direction and a decrease in amplitude of the interference structure. The transmitted rays are attenuated as they pass through the center of the sphere and thus travel inside the particle a distance equal to one sphere diameter. The super-narrow resonances correspond to much longer internal ray paths (several sphere circumferences) and are much more stronly affected by internal absorption. Therefore, measurements within super-narrow resonances can be far more sensitive to weak absorption than measurements in the "continuum" or within broader ripple features.

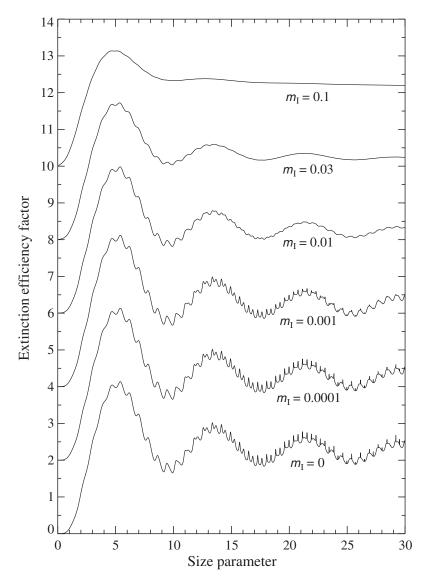
It appears that manifestations of the ripple structure can be even more spectacular in the elements of the scattering matrix than in the optical cross sections and the



**Figure 9.6.** (a) Ripple structure of extinction by a water droplet  $(m=1.33+i\times10^{-8})$  on the interval [50, 51] of size parameters. (b) High-resolution profile of the resonance  $b_{61}^1$ .

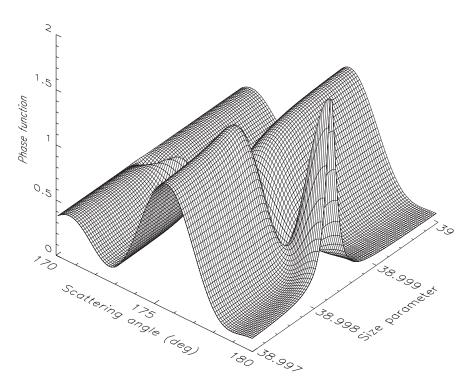
asymmetry parameter (Mishchenko and Lacis 2000). Since the normalized Stokes scattering matrix (4.65) for a fixed relative refractive index depends on two variables, viz., the size parameter x and the scattering angle  $\Theta$ , it is convenient to visualize the elements of this matrix using two-dimensional color images plotted with fine angular and size-parameter sampling resolutions.

Plate 9.1 shows the degree of linear polarization of scattered light for an unpolarized incident beam,  $P_Q = -Q^{\text{sca}}/I^{\text{sca}} = -b_1/a_1$  (%), as a function of  $\Theta$  and x for monodisperse spheres with a relative refractive index m = 1.4. This image was



**Figure 9.7.** The set of curves (bottom to top) shows the effect of increasing absorption on the interference and ripple structure of the extinction efficiency factor for monodisperse spherical particles with real part of the relative refractive index  $m_R = 1.4$ . The vertical axis scale applies to the curve with  $m_I = 0$ , the other curves being successively displaced upward by 2.

created using sampling resolutions  $\Delta\Theta=1/3^\circ$  and  $\Delta x=0.05$ . With the exception of the region of Rayleigh scattering ( $x \le 2$ ; cf. the lowest panel of Fig. 7.1), the entire polarization image is a field of sharp, alternating maxima and minima. The frequencies of the maxima and minima over both  $\Theta$  and x increase with increasing size parameter. This very complex "butterfly" structure, which appears both to be chaotic and to reveal a slightly perceptible order, was first discovered by Hansen and Travis (1974) and results from interference and resonance effects for particles of a single size. In their paper published 30 years ago, Hansen and Travis could use only white and black and, therefore, blackened the regions of positive polarization and left the



**Figure 9.8.** High-resolution surface plot of the phase function within the super-narrow resonance centered at  $x \approx 38.9983$  for monodisperse spherical particles with m = 1.4.

regions of negative polarization white. The use of the continuous color bar shown in Plate 9.1 allowed us to build a complete image of the butterfly structure with a detailed gradation of the magnitude of polarization as well as its sign.

Plate 9.2 provides a zoomed image of a small part of the field covered by Plate 9.1 and reveals with much greater detail the enormous complexity of the scattering pattern. Now the sampling resolution ( $\Delta\Theta = 0.1^{\circ}$  and  $\Delta x = 0.007$ ) is fine enough to exhibit several horizontal "dislocations" or "anomalous strips", which are first indicators of super-narrow resonances. One of these is centered at  $x \approx 38.9983$  and is shown with even greater sampling resolution ( $\Delta\Theta = 0.05^{\circ}$  and  $\Delta x = 0.00001$ ) in the top middle panel of Plate 9.3. The top left and top right panels of this plate depict the ratios  $a_3/a_1$  and  $b_2/a_1$  and demonstrate an immense degree of variability within the resonance, including drastic changes of sign and strong dependence on scattering angle. The latter is not surprising, since the corresponding resonance Lorenz–Mie coefficient contributes differently to the different expansion coefficients appearing in Eqs. (4.75)–(4.80) (see also Eqs. (4.109)–(4.114) and (5.160)–(5.162)). In consequence, its effect on the scattering matrix elements is different at different scattering angles. This conclusion is corroborated by Fig. 9.8, which shows a very strong angledependent change in the phase function  $a_1$  within the resonance, including a sharp peak at the backscattering direction.

The middle three panels of Plate 9.3 are analogous to the top three panels, but

show the degree of linear polarization computed for three increasing values of the imaginary part of the relative refractive index. Although most polarization features within the resonance gradually weaken and ultimately disappear, the super-narrow minimum located at  $\Theta \approx 177^{\circ}$  and  $x \approx 38.99828$  for  $m_{\rm I} = 0$  (the top middle panel of Plate 9.3) becomes much more pronounced and shifts toward larger  $\Theta$  and x before it finally disappears at  $m_{\rm I} = 10^{-4}$ . This behavior is quite different from that observed for  $Q_{\rm ext}$  and  $\langle \cos \Theta \rangle$  (Fig. 9.4).

The bottom three panels of Plate 9.3 show the degree of linear polarization versus  $\Theta$  and  $m_R$  for x=38.9983 and  $m_I=0$ . Interestingly, these panels are hardly distinguishable from the top three panels. This suggests again that, at least for nonabsorbing particles, the behavior of super-narrow resonances is determined by the product of the relative refractive index and size parameter rather than by each of these quantities separately. This also means that precise measurements of super-narrow resonances can be used not only for particle sizing but also for an accurate determination of the relative refractive index, provided that the particle size is already known.

A question that is naturally raised is whether the super-sharp resonances are physically "real", or are artifacts of a too-literal application of the theoretical macroscopic concept of "sphere" to microscopic objects. However, high-quality laboratory data, e.g., measurements of the intensity of light scattered by a gradually evaporating glycerol micro-droplet (Chýlek *et al.* 1992), provide an impressive experimental demonstration of the actual occurrence of this phenomenon and its practical usefulness as an optical particle-characterization tool (Section 9.7). As follows from the previous discussion, high-precision measurements within super-narrow resonances should be particularly useful for accurate particle sizing, determining the real part of the relative refractive index, and detecting minute deviations of the imaginary part of the relative refractive index from zero.

The extreme sharpness of some resonances may also help explain some of the minor, but nevertheless perplexing, differences that sometimes appear in intercomparisons of the Lorenz–Mie results for polydisperse spheres obtained by different groups (e.g., Boucher *et al.* 1998). In view of the fact that the Lorenz–Mie theory is exact, one would expect that, for given values of particle size and relative refractive index, precise agreement must be found for the resultant Lorenz–Mie parameters to many significant figures. Thus, the first step in such intercomparisons should be to verify that the Lorenz–Mie codes produce identical results for the same monodisperse size parameter and relative refractive index. Since the polydisperse scattering characteristics involve integration over a size distribution of particles (Section 3.2) with a number of integration points large enough to provide the desired numerical accuracy (Section 5.10), it is clear from the results in Figs. 9.1 and 9.4 that convergence may not be uniformly monotonic as the number of integration points is increased. Indeed, if an integration mesh point hits a sharp resonance, there may be an apparent local discontinuity that is greater than 5% compared to the background value. Hence for

precise Lorenz–Mie scattering characteristics, an exceedingly high resolution in size parameter space may be needed to resolve the resonance features fully.

### 9.2 Effects of averaging over sizes

Most natural and artificial ensembles of spherical particles do not exhibit the spikelike resonances described in the previous section because even a narrow polydispersion washes out features that strongly depend on particle size. Figure 9.9 illustrates the effect of increasing width of the size distribution on the extinction efficiency factor for the gamma size distribution, Eq. (5.245), of spherical particles with a relative refractive index m = 1.4. The figure shows  $Q_{\text{ext}} = \langle C_{\text{sca}} \rangle / \langle G \rangle$  versus effective size parameter  $x_{\text{eff}} = k_1 r_{\text{eff}}$  for five increasing values of the effective variance  $v_{\text{eff}}$ , where  $k_1$  is the wave number in the surrounding medium and  $\langle C_{\text{sca}} \rangle$  and  $\langle G \rangle$  are the ensemble-averaged scattering and geometrical cross sections per particle, respectively. The effective radius  $r_{\rm eff}$  and the effective variance  $v_{\rm eff}$  are defined by Eqs. (5.248) and (5.249) and, for the gamma distribution with  $r_{\min} = 0$  and  $r_{\max} = \infty$ , coincide with the parameters a and b of Eq. (5.245), respectively. (The computational meaning of the upper limit  $r_{\text{max}} = \infty$  was discussed in subsection 5.10.1.) Figure 9.10 demonstrates the broadening of the size distribution with increasing  $v_{\rm eff}$  while the effective radius is kept constant. Note that the size distribution with  $v_{\rm eff} = 0$  corresponds to monodisperse particles with radius  $r = r_{\text{eff}}$ , the effective variance values in the range [0.05, 0.1] are characteristic of sulfuric acid particles forming the clouds on Venus (Hansen and Hovenier 1974), and the value  $v_{\rm eff} = 0.2$  is typical of water cloud particles in the Earth's atmosphere (Mazin and Khrgian 1989).

As was the case with increasing absorption, increasing the width of the size distribution first extinguishes the ripple and then eliminates the interference structure in  $Q_{\rm ext}$ . It is in fact remarkable that as narrow a dispersion of sizes as that corresponding to  $v_{\rm eff}=0.01$  completely washes out the ripple structure. The first major maximum of the interference structure persists to larger values of  $v_{\rm eff}$ , but eventually fades away too. For distributions with  $v_{\rm eff} \ge 0.2$ , the only surviving features are the reddening at small size parameters discussed in Section 7.1 and the asymptotic geometrical optics trend  $Q_{\rm ext} \to 2$  as  $x \to \infty$  discussed in Section 7.4.

The presence of the first maximum of the interference structure for relatively narrow size distributions creates the possibility of an infrequent phenomenon for which aerosol particles of just the right size have a lower extinction efficiency factor in the blue than that at the larger wavelengths in the red. Thus, in contrast to the familiar reddening of the setting sun owing to enhanced Rayleigh scattering, a sufficiently narrow size distribution of aerosol particles in the atmosphere, with an average size such that  $4 \le 2x(m_R - 1) \le 7$  for visible wavelengths (cf. Fig. 9.3), can produce a blue cast to the sun or moon and is perhaps responsible for the implied rarity associated with the phrase, "once in a blue moon" (cf. Bohren and Huffman 1983, Chapter 4;

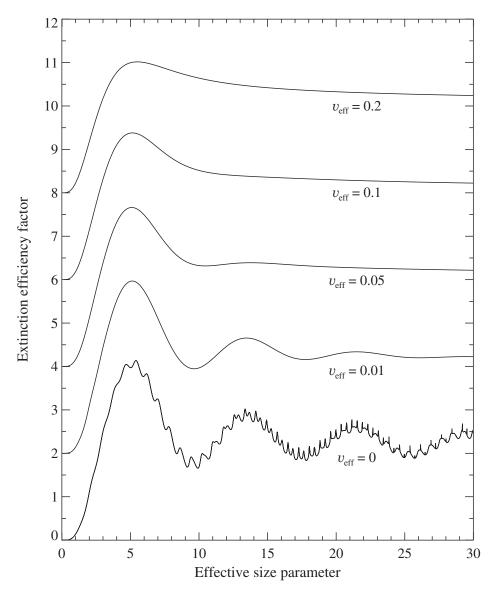


**Figure 9.9.** The effect of increasing width of the size distribution on the interference and ripple structure in  $Q_{\rm ext}$  for nonabsorbing spherical particles with relative refractive index 1.4. The vertical axis scale applies to the curve with  $v_{\rm eff} = 0$ , the other curves being successively displaced upward by 2.

#### Lynch and Livingston 1995).

Plate 9.4 shows the evolution of the linear polarization pattern with increasing width of the size distribution. The case  $v_{\rm eff} = 0.01$  demonstrates that even a very narrow size distribution is sufficient to extinguish most of the interference and resonance effects. With increasing  $v_{\rm eff}$ , the maxima are smoothed out, the minima are filled in, and the polarization becomes more neutral. Additional effects of increasing  $v_{\rm eff}$  are the depression to smaller size parameters of the region of maximal polarization corresponding to Rayleigh scattering and the erosion of the bridge of positive polarization connecting the Rayleigh region and the area of positive polarization at

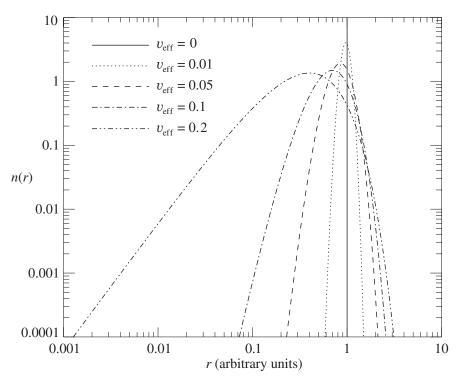


**Figure 9.10.** Gamma size distribution n(r), Eq. (5.245), with  $r_{min} = 0$ ,  $r_{max} = \infty$ ,  $r_{eff} = 1$  (in arbitrary units of length), and  $v_{eff} = 0$ , 0.01, 0.05, 0.1, and 0.2. The size distribution is normalized according to Eq. (3.26).

scattering angles around  $160^\circ$ . The island of positive polarization at  $x_{\rm eff} \sim 10$  and  $\Theta \sim 25^\circ$  for  $v_{\rm eff} = 0.01$  is an anomalous diffraction feature produced by the interference of diffracted light and light reflected and refracted by the particles in the nearforward direction (Hansen and Travis 1974). The magnitude of this feature strongly depends on the width of the size distribution: the feature significantly weakens as  $v_{\rm eff}$  increases from 0.01 to 0.07 and has completely disappeared for  $v_{\rm eff} = 0.2$ . All these effects of broadening the size distribution are easy to understand qualitatively in terms of taking weighted averages along vertical lines of increasing length in the polarization diagram for monodisperse particles.

### 9.3 Optical cross sections, single-scattering albedo, and asymmetry parameter

In the rest of this chapter we will analyze the scattering and absorption properties of polydisperse spherical particles. Most of the illustrative examples will be based on computations for the gamma distribution of particle radii with  $r_{\rm min}=0$ ,  $r_{\rm max}=\infty$ , and a fixed effective variance  $v_{\rm eff}=0.15$ . The latter is a value characteristic of a size distribution that is neither particularly narrow nor broad.

Figure 9.11 presents surface plots of the extinction efficiency factor versus effec-

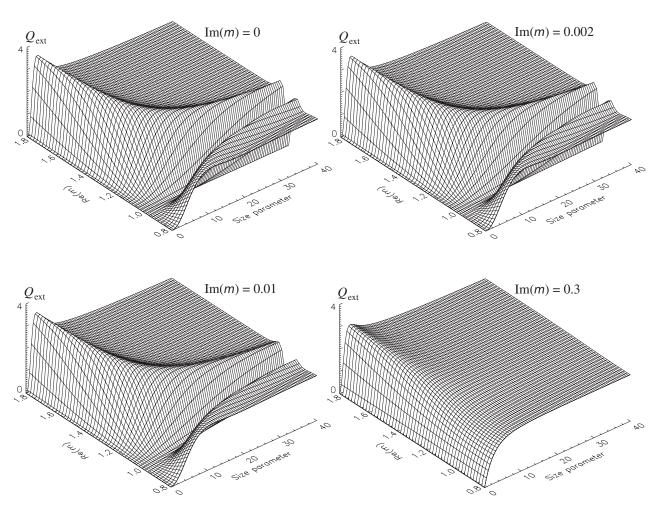


**Figure 9.11.** Extinction efficiency factor versus effective size parameter and real part of the relative refractive index for a gamma size distribution of spherical particles with  $v_{\rm eff} = 0.15$ . The imaginary part of the relative refractive index varies from 0 to 0.3.

tive size parameter and real part of the relative refractive index, for four values of the imaginary part ranging from 0 to 0.3. Figures 9.12–9.16 are analogous to Fig. 9.11 and present visualizations of the scattering and absorption efficiency factors, the single-scattering albedo, the asymmetry parameter, and the radiation-pressure efficiency factor. The 51 refractive index gridlines are drawn at 0.02 intervals and correspond to relative refractive indices  $m = 0.8, 0.82, \dots 1.78$ , and 1.8. The 81 size parameter gridlines are drawn at 0.5 intervals and correspond to size parameters  $x_{\rm eff} = 0, 0.5, 1, \dots, 39.5$ , and 40.

The upper left panel of Fig. 9.11 shows that the first interference maximum in  $Q_{\rm ext}$  indeed follows the curves  $x_{\rm eff}|m_{\rm R}-1|={\rm constant}$ , as discussed in Section 9.1. For m=1, both  $Q_{\rm ext}$  and  $Q_{\rm sca}$  vanish because there is no scattering and absorption when the particle refractive index matches that of the nonabsorbing surrounding medium. This does not mean, however, that dimensionless quantities such as the single-scattering albedo, the asymmetry parameter, and the phase function must also disap-

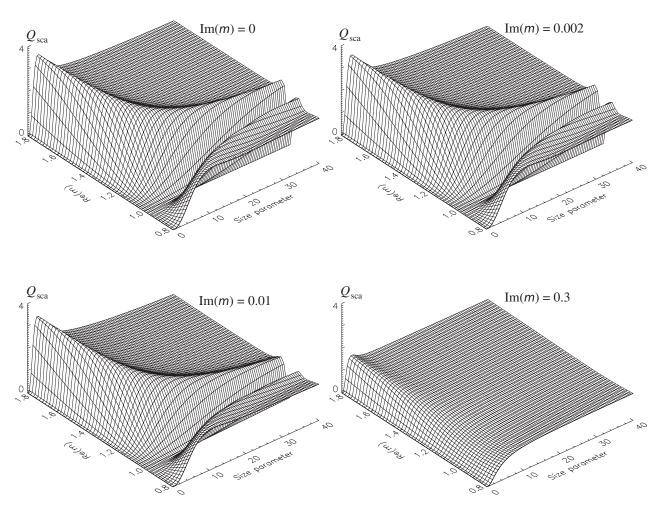


**Figure 9.12.** As in Fig. 9.11, but for the scattering efficiency factor.

pear as  $m \to 1$ . All of these are ratios of vanishing quantities and remain finite in the mathematical sense as the particle refractive index approaches that of the surrounding medium. The extinction and scattering efficiency factors tend to zero as  $x_{\rm eff} \to 0$ . In the limit  $x_{\rm eff} \to \infty$ , the extinction efficiency factor approaches the geometrical optics value 2. As  $m_{\rm I}$  increases from 0 to 0.3, the first interference maximum in both  $Q_{\rm ext}$  and  $Q_{\rm sca}$  weakens and almost disappears, except for  $m_{\rm R}$  close to 1.8. With the exception of  $m_{\rm R}$  close to unity, the scattering efficiency factor in Fig. 9.12 decreases with increasing  $m_{\rm I}$ . With either  $m_{\rm I} \to \infty$  or  $m_{\rm R} \to \infty$ ,  $Q_{\rm sca}$  for very large particles asymptotically approaches the value for a perfect reflector, i.e.,  $Q_{\rm sca} \to 2$ .

The absorption efficiency factor is zero for  $m_1 = 0$  but rapidly grows with increasing imaginary part of the relative refractive index (Fig. 9.13). It can even exceed unity in the resonance region of the size parameters, which means that a particle can absorb significantly more power than the value obtained by multiplying the incident intensity by the area of its geometrical cross section. This phenomenon shows that

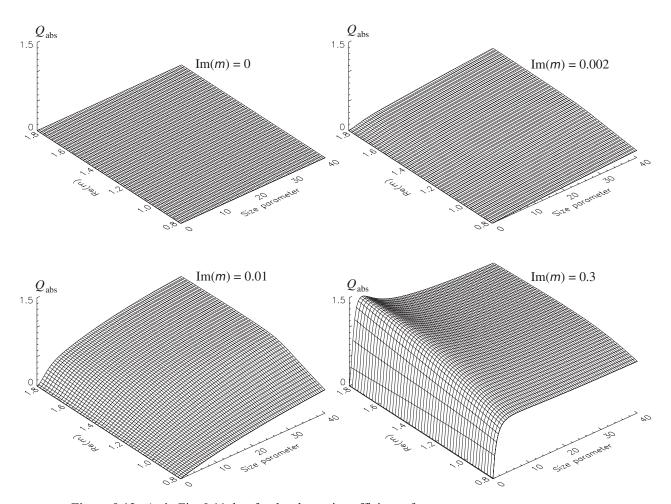


**Figure 9.13.** As in Fig. 9.11, but for the absorption efficiency factor.

spherical particles can perturb the electromagnetic field far beyond their physical confines and illustrates once again the limited applicability of the geometrical optics approximation, which predicts that the absorption efficiency factor cannot exceed unity. As  $m_I \rightarrow \infty$ , the particles become perfect reflectors, and  $Q_{abs}$  vanishes.

The single-scattering albedo is identically equal to unity for nonabsorbing particles but almost vanishes for  $m_R \approx 1$  and small  $m_I$ , because essentially all the light extracted by the particles from the incident beam is absorbed rather than scattered (the upper right and lower left panels of Fig. 9.14). As  $m_I$  deviates from zero, the single-scattering albedo vanishes in the Rayleigh region, in accordance with Eqs. (7.3) and (7.4), decreases for all  $m_R$  and  $x_{\rm eff}$ , and develops a feature resembling the first interference maximum in  $Q_{\rm ext}$  and  $Q_{\rm sca}$ . With the exception of  $m_R$ -values close to unity coupled with small or zero  $m_I$ , the single-scattering albedo depends only weakly on the real part of the relative refractive index. In the limit  $m_I \rightarrow \infty$ , the single-scattering albedo reaches the asymptotic value unity for perfectly reflecting spheres. For particles much larger than the wavelength,  $\varpi$  cannot be smaller than 0.5. Indeed, this value can only be reached when the ray-tracing scattering cross section in Eq.

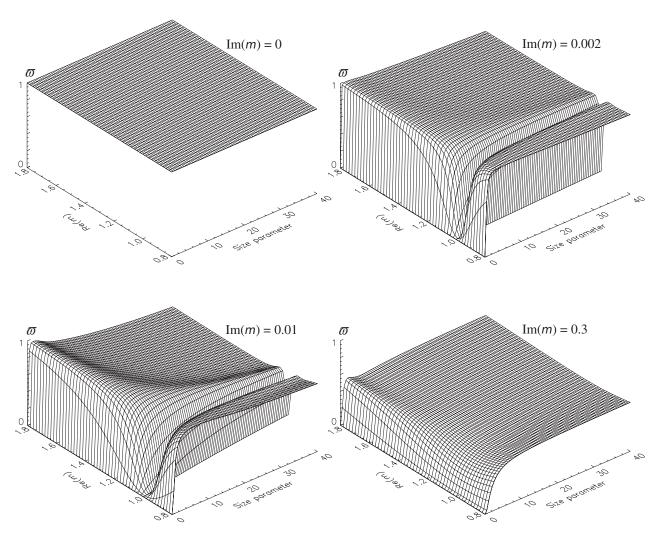


**Figure 9.14.** As in Fig. 9.11, but for the single-scattering albedo.

(7.13) vanishes, which implies that all light striking the particle is refracted into the particle and is internally absorbed.

The asymmetry parameter,  $\langle\cos\Theta\rangle$ , is zero for very small particles, in agreement with the prediction of the Rayleigh approximation, but then rapidly grows as  $x_{\rm eff}$  increases from 0 to about 2 (Fig. 9.15). Then it remains positive, thereby indicating forward-scattering particles, and shows little dependence on the particle size parameter. For particles with  $m\approx 1$ ,  $\langle\cos\Theta\rangle$  becomes independent of m and depends on the size parameter according to the Rayleigh–Gans approximation (Irvine 1963). In particular, for very large nonabsorbing particles with  $m\approx 1$ ,  $\langle\cos\Theta\rangle$  can reach values approaching unity because the diffraction lobe becomes extremely narrow, there are no reflected rays, and the incident rays striking the particle pass through it essentially undeviated. The asymmetry parameter becomes almost independent of  $m_R$  for strongly absorbing particles (lower right panel of Fig. 9.15) because the scattered light

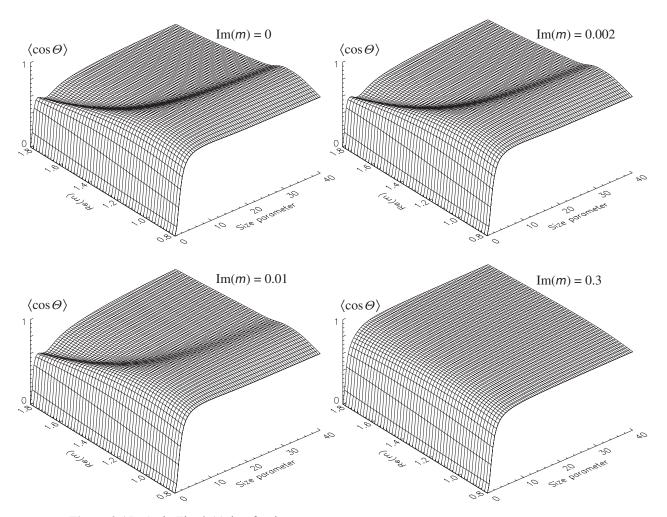


**Figure 9.15.** As in Fig. 9.11, but for the asymmetry parameter.

is dominated by the diffracted and externally reflected components. As  $m_R \to \infty$  or  $m_I \to \infty$ , the asymmetry parameter for very large particles tends to 1/2 because half the scattered radiation is diffracted in the forward direction and half is externally reflected. The reflected rays are isotropically distributed (van de Hulst 1957) and make no contribution to  $\langle \cos \Theta \rangle$ , whereas  $\langle \cos \Theta \rangle$  for the diffracted light is unity, Eq. (7.17), thereby yielding total asymmetry parameter equal to 1/2. In the limit  $x \to 0$  and  $m_R \to \infty$  or  $m_I \to \infty$ ,  $\langle \cos \Theta \rangle \to -0.4$  (van de Hulst 1957, Section 10.61).

In a similar way to the extinction and scattering efficiency factors, the radiation-pressure efficiency factor  $Q_{\rm pr}$  vanishes for very small particles and particles with  $m \approx 1$ .  $Q_{\rm pr}$  in Fig. 9.16 always increases with  $m_{\rm I}$  and, for nonabsorbing and mildly absorbing spheres, always increases as  $m_{\rm R}$  increases from 1 to 1.8. However, the dependence on the real part of the relative refractive index weakens as  $m_{\rm I}$  reaches the value 0.3. In the limit  $m_{\rm I} \rightarrow \infty$  or  $m_{\rm R} \rightarrow \infty$ , the radiation pressure efficiency factor for very large particles approaches that of a perfect reflector, i.e.,  $Q_{\rm pr} \rightarrow 1$ .

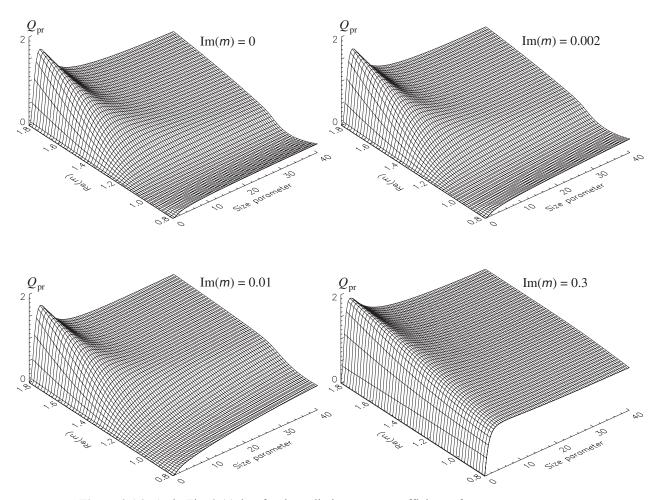
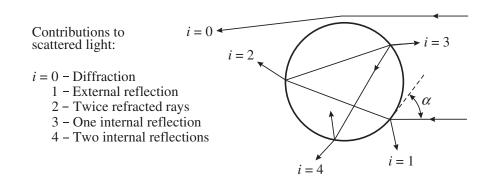


Figure 9.16. As in Fig. 9.11, but for the radiation-pressure efficiency factor.

### 9.4 Phase function $a_1(\Theta)$

Many phase function features for particles larger than the incident wavelength (Fig. 7.4) can be explained through the concepts of geometrical optics, using the terminology introduced in Fig. 9.17. Specifically, the concentration of light near  $\Theta = 0^{\circ}$  is caused by diffraction (i = 0 in Fig. 9.17). The external reflection (i = 1) does not generate any distinctive feature, whereas the twice refracted rays (i = 2) cause a broad enhancement of the phase function in the forward-scattering hemisphere.

The features in Fig. 7.4 at  $\Theta \approx 137^\circ$  and  $130^\circ$  for m = 1.33 (160° and 88° for m = 1.53) are the primary and secondary rainbows generated by i = 3 and i = 4 rays, respectively. To explain the origin of the rainbows, one needs to express the scattering angle  $\Theta$  of the emerging ray as a function of the local angle of incidence  $\alpha \in [0^\circ, 90^\circ]$  (Fig. 9.17) for  $i = 3, 4, \ldots$  This is always possible because the entire ray path remains in the plane containing the incident ray and the center of the sphere. When the derivative  $d\Theta_i(\alpha)/d\alpha$  vanishes, the scattering angle becomes nearly constant for a range of incidence angles, thereby causing an increased concentration of



**Figure 9.17.** Geometrical optics representation of scattering by a large sphere with  $m_R > 1$ . (After Hansen and Travis 1974.)

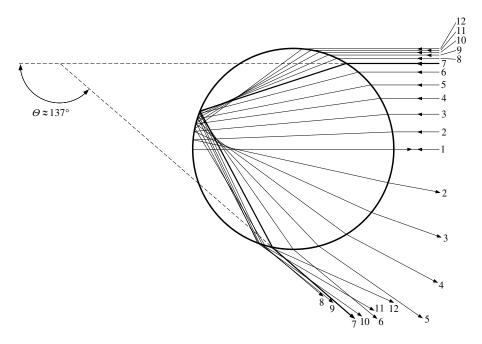


**Figure 9.18.** Ray-tracing diagram explaining the origin of the primary rainbow for a large spherical particle with m = 1.33 (after Greenler 1980). The diagram shows that incident rays corresponding to a finite range of incidence angles  $\alpha$  emerge at almost the same scattering angle, thereby creating a localized enhancement of intensity. The respective scattering angle  $\Theta \approx 137^{\circ}$  is the angle of minimum deviation for i = 3.

emerging rays. The respective scattering angle is called the rainbow angle. The condition  $d\Theta_i(\alpha)/d\alpha = 0$  implies that the rainbow angles correspond to *extrema* of the functions  $\Theta_i(\alpha)$ . Whether the extremum is a *minimum* or a *maximum* depends on *i*. The primary rainbow angle 137° for m = 1.33 (160° for m = 1.53) corresponds to a minimum in  $\Theta_3(\alpha)$  (ray 7 in Fig. 9.18), whereas the angle 130° for m = 1.33 (88° for m = 1.53) corresponds to a maximum of  $\Theta_4(\alpha)$ . As a consequence, there is a low-intensity zone (about 7° wide for m = 1.33 and 72° wide for m = 1.53) between the primary and secondary rainbows (the so-called Alexander's dark band), where the phase function is mostly determined by the externally reflected rays (i = 1). Note,

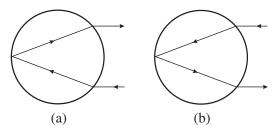


**Figure 9.19.** Rays contributing to the glory for real relative refractive indices m in the range  $2^{1/2} < m < 2$ .

however, that both rainbow angles correspond to rays that experience the least *cumulative* deviation from the initial incidence direction and hence are angles of *minimum deviation*. The slight change of the rainbow angle with wavelength caused by dispersion (change of the relative refractive index with wavelength) gives rise to the spectacular colorful rainbows often observed during showers illuminated by the sun at an altitude lower than about 40° (Lynch and Livingston 1995).

The maxima in Fig. 7.4 at  $\Theta = 119^{\circ}$  and  $141^{\circ}$  for m = 1.53 are the i = 6 and 7 rainbows, respectively. A minor feature on the large-scattering-angle side of the primary rainbow results from the interference of two i = 3 rays corresponding to different local incidence angles but emerging at the same scattering angle. This feature is called the first supernumerary bow and is not reproduced by the standard geometrical optics.

The enhancement of intensity in the backscattering direction ( $\Theta \approx 180^\circ$ ) is called the "glory" and can be seen from an airplane as a series of colored rings around the shadow cast by the airplane on a cloud top (Lynch and Livingston 1995). Obvious but relatively weak contributors to the glory are the central rays ( $\alpha = 90^\circ$ ) externally (i = 1) and internally (i = 3, 5, ...) reflected in the backscattering direction. Snell's law predicts that for real relative refractive indices in the range  $2^{1/2} \le m \le 2$ , a noncentral incident ray ( $0^\circ < \alpha < 90^\circ$  in Fig. 9.17) may emerge at  $\Theta = 180^\circ$  after just one internal reflection (i = 3, Fig. 9.19). Furthermore, the ray shown in Fig. 9.19(a) always interferes constructively with the conjugate ray propagating along the same path but in the opposite direction, Fig. 9.19(b), thereby potentially doubling the i = 3 contribution to the backscattered intensity. This contribution may partially account for the intense glory in the phase function for m = 1.53 and  $x_{\rm eff} = 600$  in Fig. 7.4.

However, this mechanism does not explain the equally pronounced glory generated by water droplets with m = 1.33 ( $< 2^{1/2}$ ) and  $x_{\rm eff} = 600$ . Therefore, it is often claimed that a major contributor to the glory is that of the edge rays ( $\alpha \approx 0^{\circ}$ ), which set up so-called surface waves on the sphere. The latter are not included in the geometrical optics formulation and are discussed by van de Hulst (1957), Nussenzveig (1992), and Grandy (2000).

Figures 9.20–9.22 illustrate the behavior of the phase function for nonabsorbing polydisperse spheres in the Rayleigh and resonance regions of the effective size

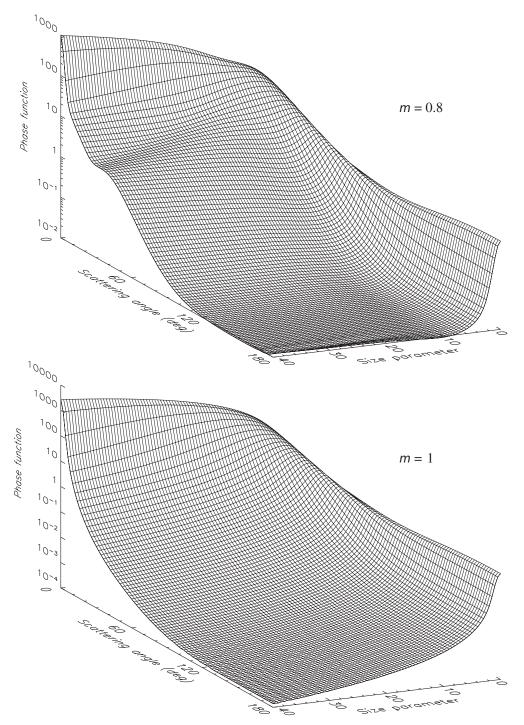


**Figure 9.20.** Phase function versus effective size parameter and scattering angle for a gamma size distribution of spherical particles with  $v_{\rm eff} = 0.15$  and two values of the relative refractive index, m = 0.8 and 1.

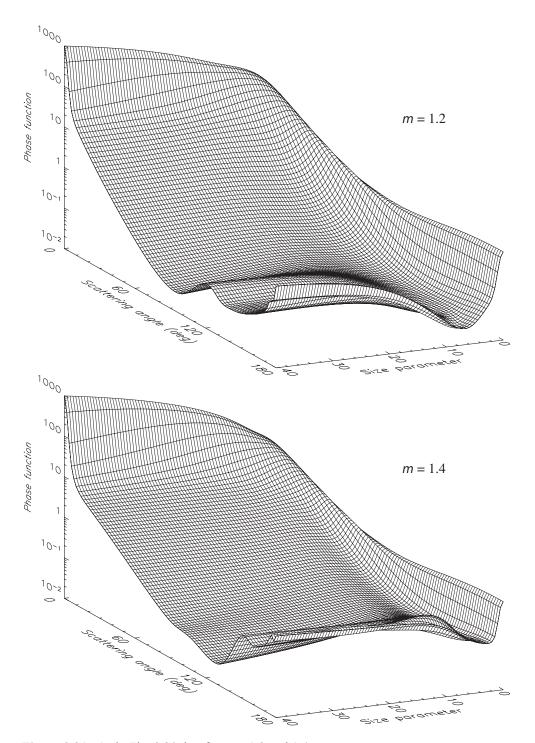


**Figure 9.21.** As in Fig. 9.20, but for m = 1.2 and 1.4.

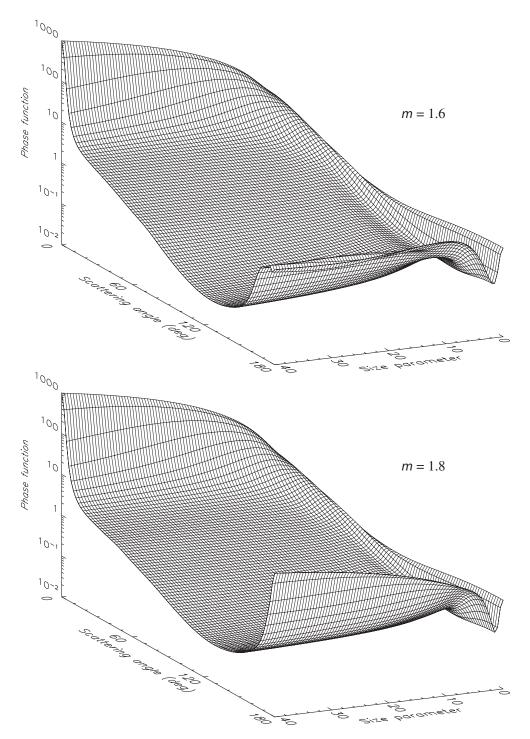


**Figure 9.22.** As in Fig. 9.20, but for m = 1.6 and 1.8.

parameter. The 91 scattering angle gridlines are drawn at  $2^{\circ}$  intervals and correspond to scattering angles  $\Theta = 0^{\circ}, 2^{\circ}, ..., 178^{\circ}$ , and  $180^{\circ}$ . The 81 size-parameter gridlines are drawn at 0.5 intervals and correspond to effective size parameters  $x_{\text{eff}} = 0, 0.5, 1, ..., 39.5$ , and 40.

In the Rayleigh limit  $x_{\text{eff}} \rightarrow 0$ , the phase functions are nearly isotropic and are given by

$$a_1(\Theta) = \frac{3}{x_{\text{eff}} \to 0} \frac{3}{4} (1 + \cos^2 \Theta)$$
 (9.9)

(see Eq. (7.5)). As the effective size parameter increases, the phase functions become anisotropic, owing to increased forward scattering and decreased backscattering. The phase functions exhibit the strongest variability with size parameter in the range  $0 < x_{\rm eff} \le 20$ . As  $x_{\rm eff}$  approaches 40, the phase functions for m = 1.2, 1.4, 1.6, and 1.8 begin to develop typical geometrical optics features such as the strong diffraction peak, the primary rainbow, and the glory. As m increases, the scattering angle of the primary rainbow increases (cf. Liou and Hansen 1971; Liou 1980) and the glory becomes more pronounced. The primary rainbow angle for m = 1.8 is so large  $(\Theta = 176^{\circ})$  that the rainbow essentially merges with the intense glory. The rainbow and the glory are absent in the Rayleigh–Gans phase function (the lower panel of Fig. 9.20) because particles with  $m \approx 1$  do not refract and reflect the incident light. For the same reason the forward-scattering peak for  $m \approx 1$  is noticeably stronger than that for the other relative refractive indices (note that in the lower panel of Fig. 9.20 the scale goes up to 10 000). The phase function in the Rayleigh–Gans limit  $m \to 1$  becomes independent of m and depends only on the size parameter (Kerker 1969). Large particles with m = 0.8 do not generate rainbows, but instead exhibit an interesting horizontal "shelf" at side-scattering angles followed by a sharp decrease of intensity at larger scattering angles. The origin of this feature for real m smaller than but close to 1 is explained in Fig. 9.23. Rays with local incidence angles  $\alpha$  > arccos m are twice refracted in the forward or near-forward directions, whereas rays with  $\alpha < \arccos m$  are totally externally reflected. The scattering angle of the externally reflected rays decreases with decreasing  $\alpha$ . Therefore,  $\Theta = 2 \arccos m$  is the critical scattering angle, beyond which the scattered intensity is expected to fall rapidly. This explanation is corroborated by Fig. 9.24, which shows the results of geometrical optics and Lorenz-Mie computations of the phase function for a gamma distribution of spherical particles with m = 0.8,  $x_{\text{eff}} = 600$ , and  $v_{\text{eff}} = 0.07$ . As expected, a sharp precipice in the phase functions occurs at  $\Theta \approx 2 \arccos(0.8) = 73.74^{\circ}$ .

Figure 9.25 demonstrates the effect of increasing absorption on the phase functions for  $m_R = 1.4$ . Comparison with the lower panel of Fig. 9.21 shows that although increasing  $m_I$  does not change the phase function for very small (Rayleigh) particles, the phase functions for larger particles become significantly smoother. The suppression of refracted rays ( $i \ge 2$ ) weakens and ultimately extinguishes the rainbow and the glory. The scattering by large particles with  $m_I = 0.3$  is dominated by diffraction and externally reflected rays, so that the phase function consists essentially of a strong

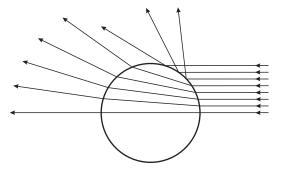


**Figure 9.23.** Ray-tracing diagram for a spherical particle with a real relative refractive index that is less than but close to unity.

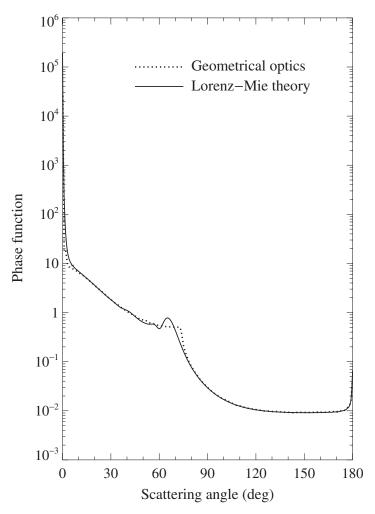


**Figure 9.24.** Geometrical optics and Lorenz–Mie phase functions for a gamma distribution of spherical particles with m = 0.8,  $x_{\text{eff}} = 600$ , and  $v_{\text{eff}} = 0.07$ .

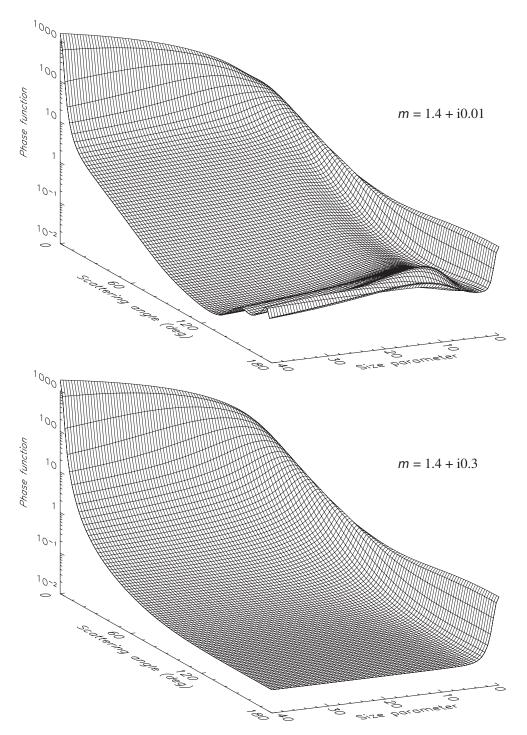


**Figure 9.25.** As in Fig. 9.20, but for m = 1.4 + i0.01 and 1.4 + i0.3.

diffraction peak in the forward direction and nearly isotropic scattering in the backward hemisphere. As a consequence, the angular profile of the phase function becomes remarkably similar to that for m = 1 (lower panel of Fig. 9.20), although the virtually zero contribution of the reflected rays in the case m = 1 makes the background phase function value in the backward hemisphere significantly lower.

### 9.5 Backscattering

Figure 9.26 shows that the phase-function value at  $\Theta = 180^{\circ}$  can vary by orders of magnitude with changing size parameter and/or real and imaginary parts of the relative refractive index. This variability makes difficult the analysis of backscattering intensity measurements and explains the large amount of attention paid by those interpreting radar and lidar observations to quantities like the average backscattering cross section per particle,

$$\langle C_{\rm b} \rangle = \left\langle \frac{\mathrm{d}C_{\rm sca}}{\mathrm{d}\Omega} \right\rangle_{\Theta = 180^{\circ}} = \frac{\langle C_{\rm sca} \rangle a_1 (180^{\circ})}{4\pi},\tag{9.10}$$

the average radar backscattering cross section per particle,

$$\langle \sigma_{\rm b} \rangle = 4\pi \langle C_{\rm b} \rangle \tag{9.11}$$

the extinction-to-backscatter ratio,

$$R_{\rm eb} = \frac{\langle C_{\rm ext} \rangle}{\langle \sigma_{\rm b} \rangle} = \frac{1}{\varpi a_1 (180^{\circ})},\tag{9.12}$$

and the backscatter-to-extinction ratio

$$R_{\rm be} = \frac{\langle \sigma_{\rm b} \rangle}{\langle C_{\rm ext} \rangle} = \varpi a_{\rm l}(180^{\circ}) \tag{9.13}$$

(e.g., Battan 1973; Reagan *et al.* 1989; Stephens 1994). The behavior of these back-scattering characteristics is illustrated in Figs. 9.27 and 9.28, which show the back-scattering efficiency factor

$$Q_{\rm b} = \frac{\langle C_{\rm b} \rangle}{\langle G \rangle} \tag{9.14}$$

and the backscatter-to-extinction ratio as a function of effective size parameter for a range of the real and imaginary parts of the relative refractive index. Note that  $Q_b$  vanishes in the limit  $m \rightarrow 1$ , because particles with the refractive index equal to that of the surrounding medium do not scatter light, whereas the dimensionless backscattering phase function and backscatter-to-extinction ratio remain finite.

A common feature of  $a_1(180^\circ)$ ,  $Q_b$ , and  $R_{be}$  is that the larger the imaginary part of the relative refractive index, the faster they reach their respective geometrical

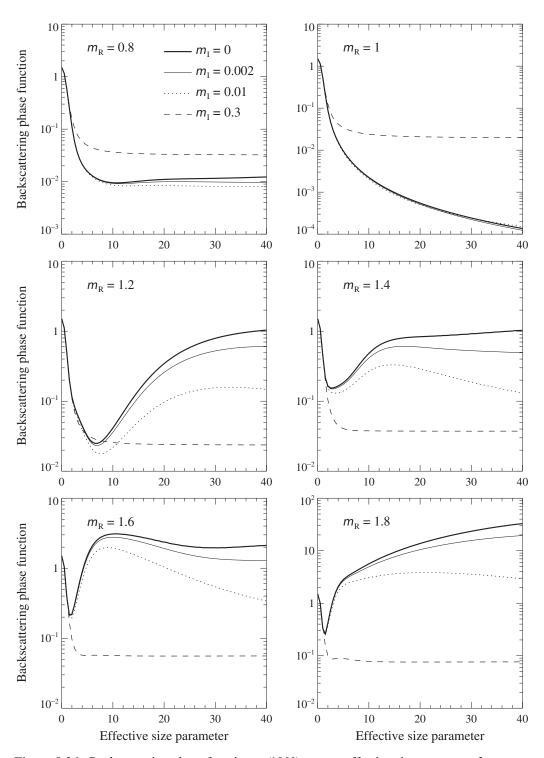


**Figure 9.26.** Backscattering phase function  $a_1(180^\circ)$  versus effective size parameter for a gamma distribution of spherical particles with  $v_{\text{eff}} = 0.15$ ,  $m_{\text{R}} = 0.8$ , 1, 1.2, 1.4, 1.6, and 1.8, and  $m_{\text{I}} = 0$ , 0.002, 0.01, and 0.3.

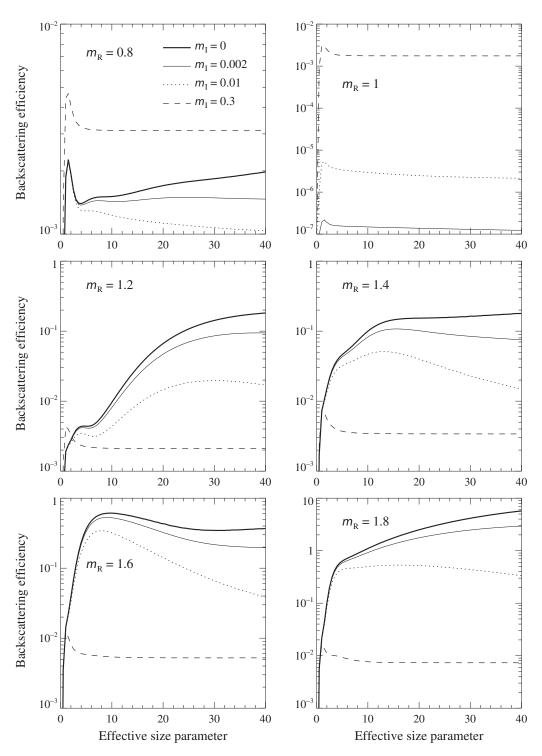


Figure 9.27. As in Fig. 9.26, but for the backscattering efficiency factor.

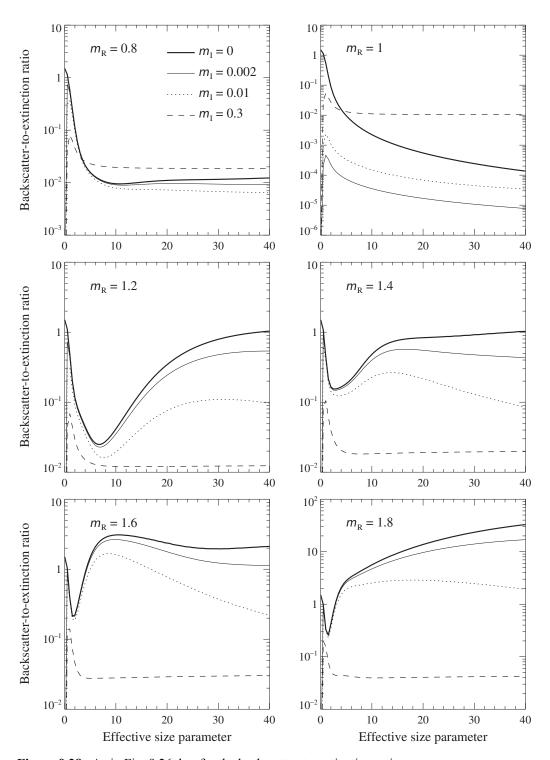


Figure 9.28. As in Fig. 9.26, but for the backscatter-to-extinction ratio.

optics limits with increasing  $x_{\rm eff}$ . An additional property of these backscattering characteristics is that they almost always decrease with increasing  $m_{\rm I}$  for  $m_{\rm R}=1.2$ , 1.4, 1.6, and 1.8. For  $m_{\rm R}=0.8$ , they first decrease as  $m_{\rm I}$  grows from 0 to 0.01 but then significantly increase as  $m_{\rm I}$  reaches the value 0.3 (except the backscatter-to-extinction ratio for  $x_{\rm eff} \le 4$ ). The backscattering phase function and the backscatter-to-extinction ratio for  $m_{\rm R} \ne 1$  have a local minimum at small effective size parameters, which is especially deep for m=1.2. The minimum becomes less pronounced and eventually vanishes with increasing absorption.

### 9.6 Other elements of the scattering matrix

Plates 9.5 and 9.6 parallel Figs. 9.20–9.22 and 9.25 and show the ratios  $a_3(\Theta)/a_1(\Theta)$ ,  $-b_1(\Theta)/a_1(\Theta)$ , and  $b_2(\Theta)/a_1(\Theta)$  (in %) versus scattering angle  $\Theta$  and effective size parameter. The use of 21 discrete colors in these contour plots (with 20 contours at  $\pm 5\%$ ,  $\pm 15\%$ , ...,  $\pm 85\%$ , and  $\pm 95\%$ ) allows the reader to quantify the diagrams using white as the reference. The ratio  $-b_1(\Theta)/a_1(\Theta)$  is the degree of linear polarization  $P_Q$  for the scattering of unpolarized incident light provided that the Stokes parameters are defined with respect to the scattering plane. Furthermore, according to Eqs. (1.112) and (4.14) the quantity  $|b_1(\Theta)|/a_1(\Theta)$  gives the degree of linear polarization  $P_L$  in the general case of the scattering of unpolarized incident light. The significance of this and the other two element ratios of the normalized Stokes scattering matrix in cases involving polarized incident light and arbitrary incidence and scattering directions follows from Eq. (4.14).

In agreement with Eqs. (4.61), (4.62), and (4.66), the ratios  $-b_1(\Theta)/a_1(\Theta)$  and  $b_2(\Theta)/a_1(\Theta)$  vanish at  $\Theta = 0^\circ$  and  $180^\circ$ , whereas  $a_3(0^\circ)/a_1(0^\circ) = 1$  and  $a_3(180^\circ)/a_1(180^\circ) = -1$ .

In the limit  $x_{\rm eff} \to 0$  Rayleigh scattering occurs. In accordance with Eq. (7.5), there is strong positive polarization with the maximal 100% value at scattering angle 90°, whereas the ratio  $b_2(\Theta)/a_1(\Theta)$  vanishes completely. The Rayleigh scattering region is similar for all relative refractive indices but is compressed to smaller size parameters for the larger values of m. The ratio  $a_3(\Theta)/a_1(\Theta)$  is antisymmetric with respect to scattering angle 90°:  $a_3(180^\circ - \Theta)/a_1(180^\circ - \Theta) = -a_3(\Theta)/a_1(\Theta)$ .

In the limit  $m \to 1$ , all three ratios become independent of size parameter and the ratio  $b_2(\Theta)/a_1(\Theta)$  vanishes. This is consistent with the well-known result of the Rayleigh-Gans approximation, that the normalized Stokes scattering matrix is given by

$$\widetilde{\mathbf{F}}_{RG}(\Theta, x_{eff}) = \psi(\Theta, x_{eff}) \begin{bmatrix} 1 + \cos^{2}\Theta & -\sin^{2}\Theta & 0 & 0 \\ -\sin^{2}\Theta & 1 + \cos^{2}\Theta & 0 & 0 \\ 0 & 0 & 2\cos\Theta & 0 \\ 0 & 0 & 0 & 2\cos\Theta \end{bmatrix}$$
(9.15)

(Kerker 1969). The degree of linear polarization and the ratio  $a_3(\Theta)/a_1(\Theta)$  are the same as for Rayleigh scattering.

In what follows we will normally omit the argument  $\Theta$  of the scattering matrix elements. The ratio  $a_3/a_1$  is almost always positive in the forward hemisphere, where it is weakly dependent on relative refractive index and size parameter. However, it shows a considerable degree of variability with m and  $x_{\rm eff}$  in the backward hemisphere. The pattern of the ratio  $b_2/a_1$  for most relative refractive indices and size parameters consists of narrow regions of positive or neutral values at small and large scattering angles separated by a wide region of negative values at side-scattering angles. Of the three ratios, the degree of linear polarization  $-b_1/a_1$  exhibits the largest degree of variability with relative refractive index and/or size parameter. This explains the remarkable potential of polarimetry as a particle characterization and remote sensing tool (Section 9.7).

With increasing  $x_{\text{eff}}$ , the scattering matrix starts to develop typical geometrical optics features. At small scattering angles the linear polarization is small because of the predominance of unpolarized diffracted light (for unpolarized incident light). Most of the light scattered in the near-forward direction is due to twice-refracted rays (i = 2) and is negatively polarized, as follows from Fresnel's equations. Externally reflected rays (i = 1) are positively polarized at all scattering angles. As m increases, the intensity of these rays increases too, especially for grazing values of the local incidence angle  $\alpha$  (Fig. 9.17), and becomes sufficient to cause a long peninsula of positive polarization values at scattering angles between  $10^{\circ}$  and  $30^{\circ}$  for m = 1.8. The steep ridge of positive polarization in the two right-hand columns of Plate 9.5 for m = 1.2, 1.4, 1.6, and 1.8 is the primary rainbow. The weaker positive feature at  $\Theta \sim$ 165° for m = 1.2 and  $\Theta \sim 110^\circ$  for m = 1.4 is the secondary rainbow. Although the secondary rainbow can be reliably identified in the polarization maps, it is barely seen in the respective phase function plots even for  $x_{\text{eff}} = 40$  (cf. Fig. 9.21). For m = 1.2the primary and secondary rainbow regions merge with the region of Rayleigh scattering, whereas for m = 1.4, 1.6, and 1.8 these regions are separated by areas of neutral or negative polarization.

The two columns on the right of Plate 9.6 illustrate the effect of increasing the imaginary part of the relative refractive index on the ratios  $a_3/a_1$ ,  $-b_1/a_1$ , and  $b_2/a_1$  for  $m_R = 1.4$ . The corresponding panels in Plate 9.5 and on the left of Plate 9.6 provide a comparison for  $m_I = 0$ . For small effective size parameters the effect of increasing  $m_I$  from 0 to 0.01 is relatively weak. For large particles the absorption of refracted rays ( $i \ge 2$ ) results in a dominance of diffracted light and externally reflected rays. The latter are positively polarized and, for m = 1.4 + i0.3, yield a polarization pattern similar to that of Rayleigh and Rayleigh–Gans scattering (compare the rightmost middle panel of Plate 9.6 with the rightmost top panel of Plate 9.5). The only significant difference is that the maximum of polarization occurs at the scattering angle  $\Theta' = 180^{\circ} - 2 \arctan m_R = 71.08^{\circ}$  rather than at 90°; here  $\arctan m_R$  is the Brewster angle. The bridge of positive  $a_3/a_1$  values at  $\Theta \sim 165^{\circ}$  fades out with

increasing  $m_{\rm I}$  and eventually disappears. As a result, the pattern of the ratio  $a_3/a_1$  for  $m=1.4+{\rm i}0.3$  also closely resembles that of Rayleigh and Rayleigh–Gans scattering (compare the rightmost top panel of Plate 9.6 with the top panel of the second column of Plate 9.5), except that the scattering angle of zero values is now  $\Theta'$  rather than 90°. The ratio  $b_2/a_1$  for large particles decreases with increasing imaginary part of the relative refractive index and almost vanishes for  $m_{\rm I}=0.3$ .

### 9.7 Optical characterization of spherical particles

As we have mentioned previously, the potentially strong dependence of the scattering properties of spherical particles on their size parameter and relative refractive index makes measurements of electromagnetic scattering a powerful noninvasive means of particle characterization. In fact, there are so many applications of optical particle characterization in laboratory and remote sensing research that simply listing them would take an inordinate amount of space. Therefore, we will describe only a few selected examples, directing the reader for more details and further references to the books by Kerker (1969), Bayvel and Jones (1981), Gouesbet and Gréhan (1988), Stephens (1994), and Xu (2000), the feature journal issue edited by Hirleman and Bohren (1991), and the recent review by Jones (1999).

The lower curve in Fig. 9.29 depicts measurements of the intensity of the light scattered by a slowly evaporating glycerol droplet at a scattering angle of approximately 90°. The droplet was illuminated by a linearly polarized laser beam at a wavelength  $\lambda_1 = 0.5145 \,\mu\text{m}$ , the same beam being used to levitate the particle. The upper curve shows the results of Lorenz-Mie computations for a spherical droplet with a radius ranging from 4.38 to 4.67 μm and a relative refractive index of 1.4746 corresponding to that of glycerol at the visible wavelength. Comparison of the two curves demonstrates that by identifying the locations of the resonance features in the experimental data the diameters of spherical droplets can be determined with extreme precision. Chýlek et al. (1983) developed a technique for determining the relative refractive index as well as the size of an optically levitated spherical particle illuminated by a tunable dye laser. The technique is based on analyzing both the wavelengths of the resonance peaks and the line profiles in the curve of the backscattered intensity as a function of laser wavelength. More recent developments have been described by Huckaby et al. (1994), Ray and Nandakumar (1995), and Tu and Ray (2001).

We already discussed in Section 8.1 the use of measurements of the Stokes scattering matrix for sizing polydisperse water droplets (cf. Fig. 8.2). Figure 9.30 illustrates another application of this technique. The solid curves depict ratios of the elements of the normalized Stokes scattering matrix measured by Bottiger *et al.* (1980) in the scattering-angle range  $12^{\circ} \le \Theta \le 165^{\circ}$  for a spherical latex particle. As the source of light, Bottiger *et al.* used a He–Cd laser operating at a wavelength 441.6

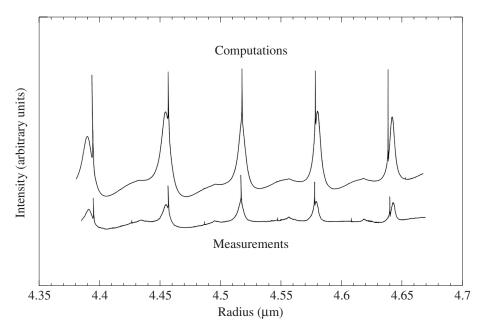


**Figure 9.29.** Measurements and computations of the intensity (in arbitrary units) scattered by a glycerol droplet at a scattering angle of approximately 90° versus droplet radius (after Chýlek *et al.* 1992).

nm. The electrostatic levitation technique allowed them to select a single particle and trap it in a very small volume. Bottiger et al. did not measure the size of the particle and only indicated that the average diameter of latex microspheres used in their experiments was 1091 nm with standard deviation 8 nm. The results of monodisperse Lorenz-Mie computations for the diameter 1091 nm and relative refractive index of latex in air 1.588 showed no resemblance to the Bottiger et al. data (Mishchenko and Mackowski 1996). However, a very good agreement was found for the diameter 1122 nm, as demonstrated in Fig. 9.30 by the dotted curves. Although Bottiger et al. did not specify the magnitude of their experimental errors, the latter can perhaps be inferred by comparing the experimental curves for the ratios  $a_3/a_1$  and  $a_4/a_1$ , which must be the same for homogeneous spherical particles. Despite some residual differences between the experimental data and the results of theoretical computations, the numbers of major maxima and minima in the solid curves and their locations are reproduced almost perfectly. The dotted curves in the left- and right-hand panels of Fig. 9.31 were computed for diameters 1108 and 1136 nm, respectively, and deviate significantly from the experimental curves. This demonstrates that the accuracy of sizing the latex particle using measurements of the Stokes scattering matrix is better than  $\pm 14$  nm or 1.2%.

The final example illustrates the use of polarimetry for remotely retrieving cloudparticle microphysics and represents what is perhaps the most spectacular achievement of planetary remote sensing. Figures 9.32 and 9.33 show the results of groundbased measurements of the linear polarization of sunlight reflected by Venus as a

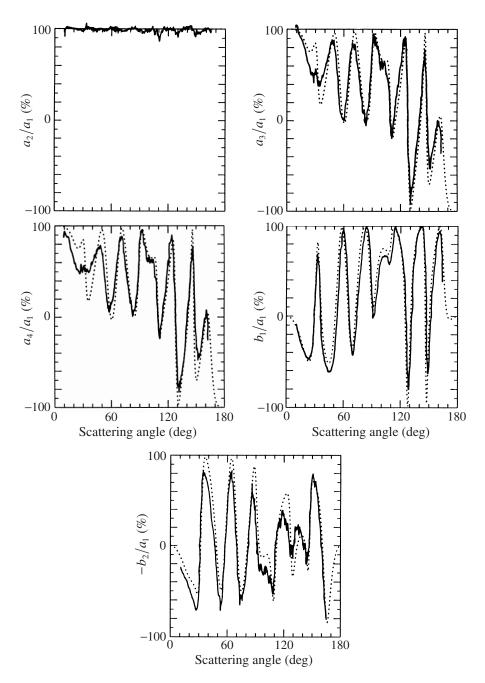


**Figure 9.30.** Ratios of the elements of the normalized Stokes scattering matrix for a single latex sphere. The solid curves depict the laboratory data by Bottiger *et al.* (1980), whereas the dotted curves show the results of Lorenz–Mie computations for the sphere diameter 1122 nm.

function of scattering angle at wavelengths 0.55 and 0.99  $\mu m$ , respectively. The curves depict the results of theoretical calculations based on a simple model of the Venus atmosphere in the form of a homogeneous, optically semi-infinite, locally plane-parallel cloud layer uniformly covering the entire planet (Hansen and Hovenier 1974). The cloud particles were assumed to be spherical, and their single-scattering

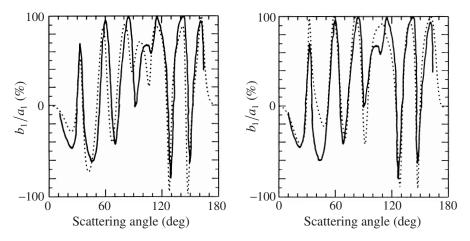


Figure 9.31. As in Fig. 9.30, but for diameters 1108 nm (left panel) and 1136 nm (right panel).

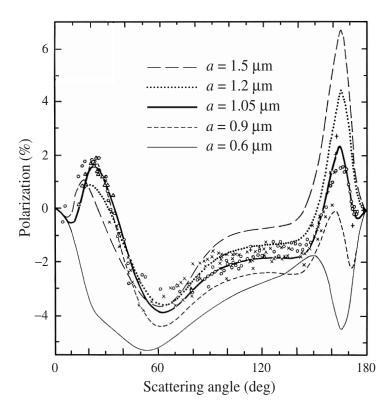


Figure 9.32. Observations of the polarization of sunlight reflected by Venus in the visual wavelength region (symbols) and theoretical computations at  $0.55 \,\mu m$  wavelength (curves). The theoretical results are based on a model of nonabsorbing spherical particles with fixed relative refractive index (m = 1.44) and fixed effective variance of the size distribution ( $v_{\rm eff} = 0.07$ ) (curves). The different curves show the influence of the effective radius  $a \equiv r_{\rm eff}$  on the polarization. (After Hansen and Hovenier 1974.)

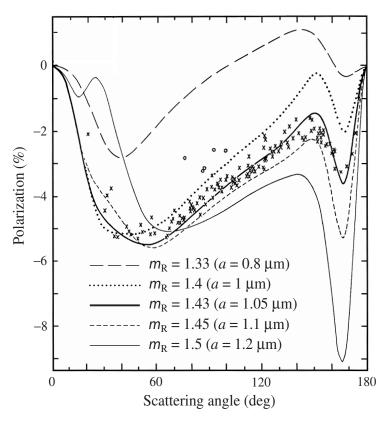


Figure 9.33. Observations (symbols) and theoretical computations (curves) of the polarization of the sunlight reflected by Venus at  $0.99 \,\mu m$  wavelength. The different theoretical curves are for various relative refractive indices, the effective radius being selected in each case to yield the closest agreement with the observations. The effective variance of the cloud-particle size distribution is fixed at 0.07. (After Hansen and Hovenier 1974.)

properties were modeled using the Lorenz–Mie theory. The computations of multiple scattering of light in the atmosphere were based on the so-called adding/doubling procedure for the numerical solution of the vector radiative transfer equation (Hovenier 1971; Hansen and Travis 1974). Hansen and Hovenier used the simple gamma distribution (5.245) to represent analytically the distribution of cloud particles over sizes and found the parameters  $a = r_{\text{eff}}$  and  $b = r_{\text{eff}}$  of this distribution, as well as the relative refractive index, by minimizing the differences between the observational data and the results of model computations. From the comparisons between the computed and observed quantities, Hansen and Hovenier deduced the following.

The observations can indeed be reproduced quantitatively using a model of nonabsorbing spherical particles. The observational data at visible wavelengths contain a clear signature of the spherical particle shape, such as the primary rainbow at  $\Theta \sim 160^\circ$  and the anomalous diffraction feature at  $\Theta \sim 25^\circ$  (cf. Fig. 9.32 and the lower left panel of Plate 9.4). This interpretation is confirmed by the spectral variation of the observed polarization.

- The effective radius of the cloud particles is  $1.05 \pm 0.10 \,\mu\text{m}$ .
- The particle size distribution is narrow, with an effective variance  $v_{\text{eff}} = 0.07 \pm 0.02$ .
- The cloud-particle refractive index has a normal dispersion, decreasing from  $1.46 \pm 0.015$  at a wavelength  $0.365 \, \mu m$  to  $1.43 \pm 0.015$  at a wavelength  $0.99 \, \mu m$ .

Based on the spectral dependence of the refractive index, Hansen and Hovenier concluded that the cloud particles consist of a concentrated (76% by weight) aqueous solution of sulfuric acid ( $H_2SO_4 - H_2O$ ). This remarkable result has been confirmed by subsequent *in situ* measurements and observations from Venus-orbiting satellites (e.g., Sato *et al.* 1996 and references therein).

### **Further reading**

Scattering phenomena associated with homogeneous spherical particles are extensively discussed in van de Hulst (1957), Nussenzveig (1992), Lynch and Livingston (1995), and Grandy (2000). An overview of scattering and absorption properties of layered and radially inhomogeneous spherically symmetric particles can be found in the books by Kerker (1969), Prishivalko *et al.* (1984), and Babenko *et al.* (2003).

The use of laboratory measurements of scattering matrix elements for sizing spherical particles is described by Maltsev *et al.* (1997) and Kaplan *et al.* (2000). The book edited by Gehrels (1974) contains many applications of polarimetry to particle characterization in astrophysics and planetary remote sensing. The use of polarimetry in remote sensing of the terrestrial atmosphere is described by Brogniez *et al.* (1992), Buriez *et al.* (1997), Mishchenko and Travis (1997), Deuzé *et al.* (2000), Masuda *et al.* (2000), Sano and Mukai (2000), and Chowdhary *et al.* (2001). Dubovik and King (2000) and Lacis *et al.* (2000) discussed the retrieval of microphysical properties of spherical aerosols using multi-wavelength measurements of extinction and sky radiances. The characterization of water-cloud droplets and spherical aerosol particles using radiance measurements from space is reviewed by Nakajima and King (1990), King *et al.* (1999), and Rossow and Schiffer (1999).